nature portfolio

https://doi.org/10.1038/s41586-023-06279-y

Supplementary information

Spin-mediated shear oscillators in a van der Waals antiferromagnet

In the format provided by the authors and unedited

Supplementary Information for "Spin-mediated shear oscillators in a van der Waals antiferromagnet"

Supplementary Note 1. Crystal structure of $FePS_3$

In Fig. 1a of the main text, only the Fe atoms in the crystal structure of $FePS_3$ are shown to highlight the arrangement of magnetic moments. We plot the full crystal structure in Supplementary Fig. 1 that includes all atoms.

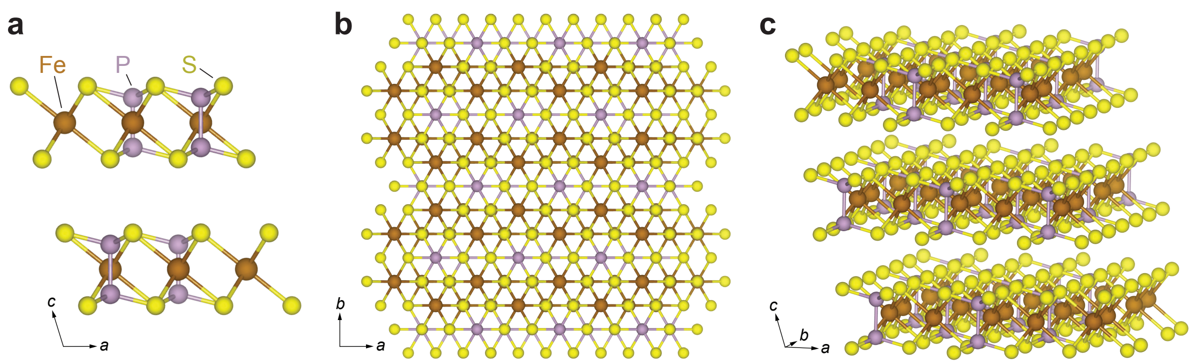

Supplementary Figure 1. Schematics of $FePS_3$ crystal structure in the a-c plane (projected along $\mathbf{b}^*$, panel **a**), in the a-b plane (projected along $\mathbf{c}^*$, panel **b**), and a 3D view (panel **c**). Graphics rendered by VESTA[71].

Supplementary Note 2. Relation between reciprocal-space tilt and real-space shear

In the main text, we stated that a rotation of Friedel pairs relative to the undiffracted (0 0 0) peak in reciprocal space can be caused by either a rotation or shear in real space, and the former is excluded because the mode frequency is independent from the lateral size of micro-patches in the film (Extended Data Fig. 5). While a real-space rotation is straightforward to understand, a real-space shear can also cause a reciprocal lattice tilt because it rotates the out-of-plane unit cell vector (vector $\mathbf{c}$ in Fig. 1a) and hence rotates the reciprocal lattice unit vector $\mathbf{a}^*$ (Fig. 1e). In this section, we quantitatively establish how real-space shear is related to reciprocal-space tilt.

Consider the interlayer shear depicted in Supplementary Fig. 2a; note that this schematic only illustrates the shear component of the film motion while other possible photoinduced acoustic modes, such as the interlayer breathing mode, are not drawn. If

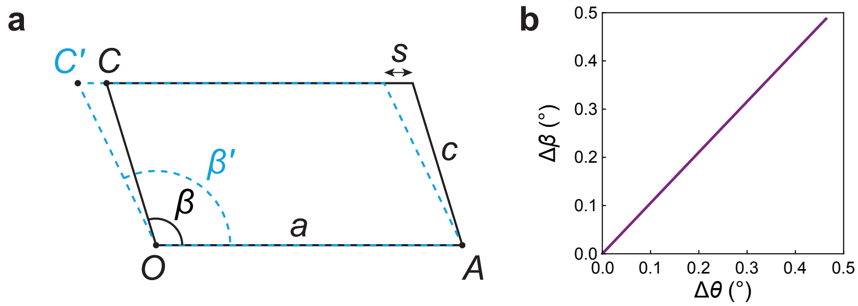

Supplementary Figure 2. **a**, Schematic of interlayer shear-induced change in the monoclinic angle, β. Drawings are exaggerated for visual clarity and are not to scale. **b**, Change in the monoclinic angle ($\Delta\beta$) as a function of the seesaw tilt ($\Delta\theta$) of ($\pm 3\ \mp 3\ \mp 1$) peaks due to the interlayer shear depicted in **a**.

the original real-space monoclinic unit cell is defined by lattice parameters a, b, c and β ($\alpha = \gamma = 90°$), in the Cartesian coordinates, the three primitive unit cell vectors are $\overrightarrow{OA} = (a, 0, 0)$, $\overrightarrow{OB} = (0, b, 0)$ (not drawn), and $\overrightarrow{OC} = (c\cos\beta, 0, c\sin\beta)$. For the ($H\ K\ L$) peak in reciprocal space that corresponds to a fixed orientation of the crystal in real space, the scattering vector is given by

$$\mathbf{q} = 2\pi\left(\frac{H}{a}, \frac{K}{b}, \frac{1}{\sin\beta}\left(\frac{L}{c} - \frac{H}{a}\cos\beta\right)\right). \tag{S1}$$

Under interlayer shear by a displacement s, $\overrightarrow{OC}$ becomes $\overrightarrow{OC'} = (c\cos\beta - s, 0, c\sin\beta)$. The scattering vector for peak ($H\ K\ L$) is updated to be

$$\mathbf{q}' = \mathbf{q} + \delta\mathbf{q}, \text{ where } \delta\mathbf{q} = \left(0, 0, \frac{2\pi}{\sin\beta}\frac{Hs}{ac}\right). \tag{S2}$$

Note that $\delta\mathbf{q}$ is odd in the Miller index H, so pairs of peaks with $\pm H$ have opposite shifts in reciprocal space along the out-of-plane L direction. In other words, the effect of interlayer shear is to cause an out-of-plane seesaw tilt $\Delta\theta$ for diffraction peaks with nonzero H, where the plane is defined by the basal plane of the honeycomb $FePS_3$ lattice. Another consequence of the interlayer shear is a change in the monoclinic angle, from β to $\beta' = \arctan\left(\frac{c\sin\beta}{c\cos\beta - s}\right)$. In Supplementary Fig. 2b, we plot the tilting angle $\Delta\theta$ of the ($\pm 3\ \mp 3\ \mp 1$) peaks as a function of $\Delta\beta \equiv \beta' - \beta$, showing a quasi-linear relation with a constant of proportionality close to unity. Therefore, the change in this monoclinic angle $\Delta\beta$ can be a good proxy for the tilting angle $\Delta\theta$ of the reciprocal lattice peaks as a result of the interlayer shear.

Supplementary Note 3. Distinction between interlayer breathing and interlayer shear

We stated in the main text that the observed out-of-phase intensity oscillation within a Friedel pair does not arise from the conventional interlayer breathing mode, which manifests as a longitudinal strain wave bounced between the opposite film surfaces. Here, we provide a more detailed justification for this statement. The interlayer breathing mode causes an oscillatory motion of the reciprocal lattice points in high-order Laue zones while leaving the points in the zeroth-order Laue zone (ZOLZ) stationary; this scenario is illustrated in Supplementary Fig. 3a. To observe this breathing mode, sample tilting is necessary because it enables us to access peaks in higher-order Laue zones[37,38], as illustrated in Supplementary Fig. 3b. However, whether the oscillations within a Friedel pair are out of phase or in phase sensitively depends on the tilt angle.

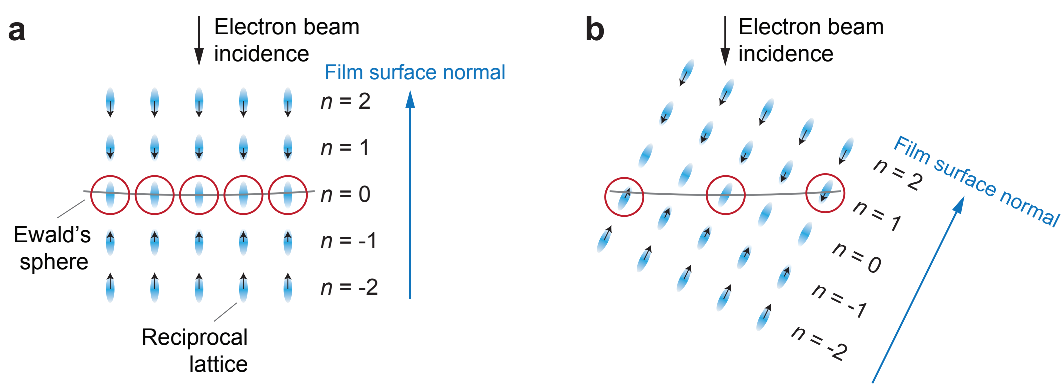

Supplementary Figure 3. Effect of interlayer breathing mode on the reciprocal lattice. **a**, Displacement of reciprocal lattice rel-rods, as indicated by the arrows, during an out-of-plane lattice expansion in real space. The Laue zone order is denoted by n, and the reciprocal lattice is drawn for a 2D rectangular lattice for simplicity. Peaks that intersect with the Ewald's sphere are circled. As these peaks are in the ZOLZ, they do not move, hence their diffraction intensity unchanged. **b**, If peaks in higher-order Laue zones are detected due to large sample tilting, interlayer breathing can lead to intensity modulation for a Friedel pair that intersects the Ewald's sphere at some specific tilt angle.

In our experiments, the diffraction peaks measured are in the ZOLZ, yet they still execute out-of-phase intensity oscillation within a Friedel pair. We note that the L Miller index is not zero in our case due to the monoclinic unit cell of $FePS_3$. The measured peaks in Figs. 1–3, such as $(\mp 3\ \ \pm 3\ \ \pm 1)$, are in the ZOLZ for the [1 0 3] zone axis; see the real and reciprocal space geometry illustrated in Extended Data Fig. 2a,b. Since these ZOLZ peaks are sensitive to the atomic motion along the in-plane but not along the out-of-plane direction, the observed lattice dynamics are not the interlayer breathing mode.

Supplementary Note 4. Change of the monoclinic angle upon demagnetization

In Fig. 4b of the main text, we explicitly measured the photoinduced change in β using time-resolved X-ray diffraction. This was done by tracking how Bragg peaks (0 0 2) and ($\bar{2}$ 0 2) move in reciprocal space. Supplementary Figure 4a shows the typical behavior of the two peaks in the antiferromagnetic state, where both experience a transient shift along the $\mathbf{c}^*$ axis but in opposite directions. As illustrated in Supplementary Fig. 4b, the peak shifts correspond to a transient reduction in β, where $\Delta\beta$ can be computed using simple trigonometry based on the relative movement of (0 0 2) and ($\bar{2}$ 0 2) peaks. The resulting evolution of $\Delta\beta$ is shown in Fig. 4b in the main text, featuring an instantaneous decrease followed by an exponential relaxation process. We note that the exact timescales exhibited in the $\Delta\beta$ evolution are strongly dependent on temperature and sample thickness[26]; nonetheless, the recovery timescale is typically beyond tens of nanoseconds, accounting for the nearly-flat plateau p_0 in ultrafast electron diffraction and microscopy, where the pump-probe delay window is below 1 ns (Figs. 1c, 1g, and 2a).

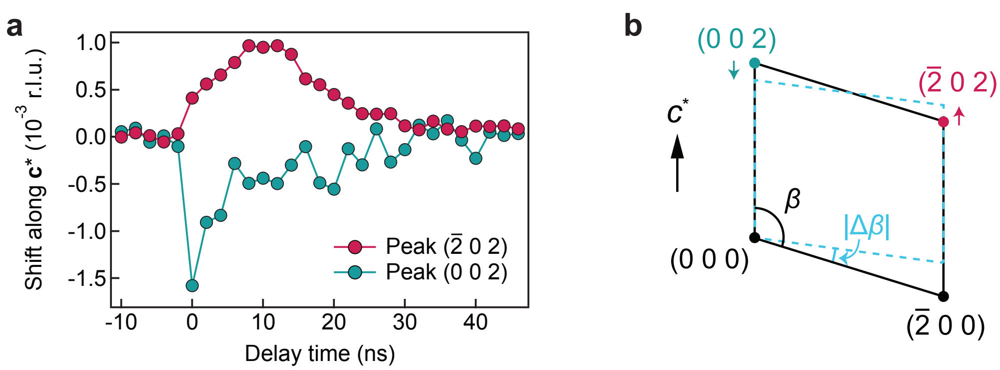

Supplementary Figure 4. **a**, Position shifts of (0 0 2) and ($\bar{2}$ 0 2) Bragg peaks following excitation at 400 nm at 100 K. Both shifts are along the $\mathbf{c}^*$ axis. **b**, Illustration of the relation between a change in the β angle and the shifts of (0 0 2) and ($\bar{2}$ 0 2) peaks. Dashed parallelogram represents the transient reciprocal lattice where $\Delta\beta$ is exaggerated.

Based on our equilibrium and time-resolved X-ray measurements, the monoclinic angle β always decreases when the antiferromagnetic order is lost. Why does β decrease but not increase upon demagnetization? Without resorting to *ab initio* calculations to quantify the spin-lattice interaction, we provide an intuitive answer based on the fact that the zigzag antiferromagnetic order always follows the monoclinic stacking direction, namely, the zigzag spin chains are along the a-axis (Fig. 1a). In a hypothetical case of β approaching 90° (the actual β value is around 107°; see Extended Data Fig. 9d), the zigzag order is expected to be degenerate along the three equivalent in-plane directions, hence reducing its strength along the original a-axis. Since the equilibrium β value is greater than 90° to break the threefold symmetry, we expect an increasing β to correlate with an enhancement of the zigzag spin order along the a-axis; hence, demagnetization corresponds to a decrease in β.

It is also worth noting that even though both the spin order and β angle changes at T_{N} or after photoexcitation, the primary order parameter is still the zigzag magnetic moment. This is because the magnetic transition in $FePS_3$ persists down to a monolayer[21,72] where β is no longer defined, so interlayer shear is a linearly coupled degree of freedom to the lowest order[26].

Supplementary Note 5. Coherent shear oscillations in $FePSe_3$

While the experiments presented in the main text focused on $FePS_3$, other 2D magnets with weak interlayer van der Waals interaction are expected to support similar susceptibility to shear as in $FePS_3$ and thus host a similar gigahertz seesaw oscillation in their reciprocal lattice. One candidate material is $FePSe_3$, a close cousin of $FePS_3$. The reported T_{N} values of $FePSe_3$ fall within the range between 112 K and 123 K[73–75], which is close to that of $FePS_3$ ($T_{\mathrm{N}} \approx 117$ K). In addition, both compounds share a zigzag antiferromagnetic order within the honeycomb lattice of Fe ions, where the magnetic moment is aligned in the out-of-plane direction. The magnitudes of their out-of-plane magnetic moment are also similar: $4.52(5)\mu_B$ for $FePS_3$ and $4.9\mu_B$ for $FePSe_3$, where μ_B is the Bohr magneton[29,74].

Despite the similarities, one important difference between $FePS_3$ and $FePSe_3$ is their distinct lattice structures (Supplementary Fig. 5). In both compounds, Fe ions in each layer form a honeycomb lattice, but the layer stackings are different. The nonmagnetic unit cell of $FePS_3$ has a monoclinic structure (space group No. 12), where neighboring layers are stacked with a shear along the a-axis, leading to $\alpha = \gamma = 90°$ and $\beta \approx 107°$. On the other hand, the adjacent honeycomb lattice of Fe in $FePSe_3$ has an AB-type stacking. In this case, half of the Fe ions lie directly over the center of a hexagon in adjacent layers, leading to a rhombohedral unit cell (space group No. 148), with $\alpha = \beta = 90°$ and $\gamma = 120°$.

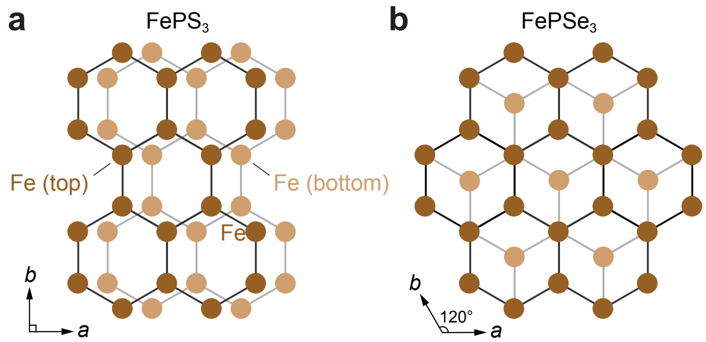

Supplementary Figure 5. Comparison of lattice structures of $FePS_3$ (**a**) and $FePSe_3$ (**b**). Only the Fe atoms are shown, and the structures are drawn in the projection along the $\mathbf{c}^*$ axis onto the a-b plane. While $FePS_3$ has a monoclinic stacking with $\beta \approx 107°$, $FePSe_3$ has an AB-type stacking with $\beta = 90°$.

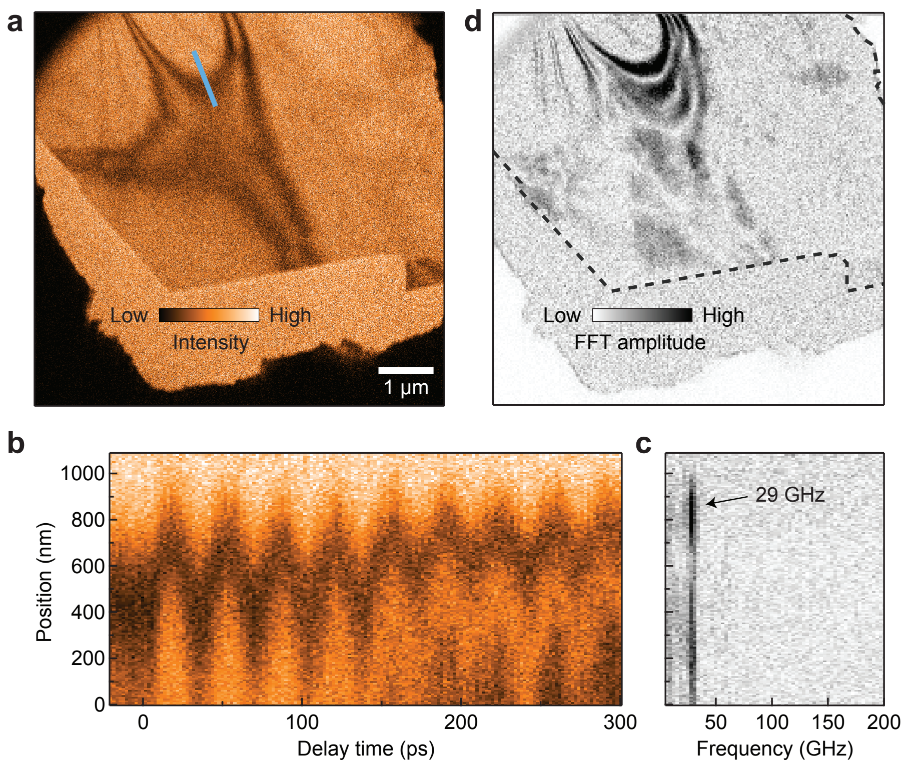

Supplementary Figure 6. Contour oscillation in the antiferromagnetic phase of $FePSe_3$. **a**, Static transmission electron micrograph of a free-standing $FePSe_3$ flake suspended from standard TEM copper mesh grid (black boundaries). Similar to $FePS_3$, dark curves are bend contours due to flake curvature. **b**, Position oscillations of the bend contour along the blue line cut in **a** following 515-nm photoexcitation at 98 K with an incident fluence of 2.4 $\mathrm{mJ\,cm^{-2}}$. **c**, Fourier transform spectra along the time-axis for panel **b**, featuring a single 29 GHz mode throughout the line cut as the corresponding bend contour oscillates in space. **d**, Spatial distribution of Fourier transform amplitude of the 29 GHz mode associated with the photoinduced contour oscillation (see Supplementary Video 2). Dashed curve demarcates the sample boundary.

An equilibrium transmission electron micrograph of $FePSe_3$ at 98 K is shown in Supplementary Fig. 6a. The bend contours in this image start to execute a similar oscillation in position after the incidence of a 515-nm pump pulse (Supplementary Video 2), which is absent above T_N. To compare the bend contour oscillations between $FePSe_3$ and $FePS_3$, we employed the same pump fluence (2.4 $\mathrm{mJ\,cm^{-2}}$) and examined the contour displacement along a particular line cut (Supplementary Fig. 6b). The oscillatory dynamics again show a cosine-like profile, indicative of the displacive mechanism of its excitation. The bend contour oscillation consists of a single mode at 29 GHz, as revealed by the Fourier transform spectra along the line cut in Supplementary Fig. 6c. To visualize this mode in space, we plot the Fourier transform amplitude of intensity oscillation for individual pixels in the electron micrograph (Supplementary Fig. 6d). The nonzero mode intensity around all visible bend contours in this sample indicates that the mode is not limited to specific boundary conditions but instead permeates throughout the sample.

In summary, despite their distinct crystal structures, the observation of seesaw oscillation of reciprocal lattice in both $FePS_3$ and $FePSe_3$ suggests the important role of interlayer shear — which can be much more readily modified in van der Waals magnets than in 3D magnets — in driving this mechanical resonance.

Supplementary Video 1. Spatially-resolved photoinduced shear oscillation in $FePS_3$ visualized by ultrafast electron microscopy

The video shows photoinduced shifts in the bend contours below and above the Néel temperature, displaying pronounced oscillation only in the antiferromagnetic state. In the movie taken at 98 K, white dashed curves mark a pair of stationary contours corresponding to the (0 ±6 0) peaks. The 515-nm pump laser had an incident fluence of 2.4 $\mathrm{mJ\,cm^{-2}}$ and the data was taken with a 200-keV electron beam.

Supplementary Video 2. Photoinduced shear oscillation in $FePSe_3$

The video shows a similarly pronounced contour position oscillation in the antiferromagnetic state of $FePSe_3$, taken at 98 K with the same pump and probe condition as that in Supplementary Video 1.

Supplementary Video 3. Simulated film motion following photoexcitation

The video shows the instantaneous velocity (**a**), horizontal displacement (**b**), vertical displacement (**c**), angular momentum (**d**), and interlayer shearing angle (**e**) of each coarse-grained region in a free-standing thin film, following a photoexcitation event at the zeroth time step. The film is depicted in the *a*-*c* plane. Angular momentum is computed with respect to the axis going out of the page at the film center of mass. Displacement values are normalized with respect to the horizontal or vertical spacing between adjacent blocks. See the Methods section for simulation details.

Supplementary References

[71] K. Momma and F. Izumi, VESTA 3 for three-dimensional visualization of crystal, volumetric and morphology data, J. Appl. Crystallogr. **44**, 1272 (2011).

[72] J.-U. Lee, S. Lee, J. H. Ryoo, S. Kang, T. Y. Kim, P. Kim, C.-H. Park, J.-G. Park, and H. Cheong, Ising-type magnetic ordering in atomically thin $FePS_3$, Nano Lett. **16**, 7433 (2016).

[73] G. Le Flem, R. Brec, G. Ouvard, A. Louisy, and P. Segransan, Magnetic interactions in the layer compounds $M\mathrm{P}X_3$ (M = Mn, Fe, Ni; X = S, Se), J. Phys. Chem. Solids **43**, 455 (1982).

[74] A. Wiedenmann, J. Rossat-Mignod, A. Louisy, R. Brec, and J. Rouxel, Neutron diffraction study of the layered compounds $MnPSe_3$ and $FePSe_3$, Solid State Commun. **40**, 1067 (1981).

[75] Y. Wang, J. Ying, Z. Zhou, J. Sun, T. Wen, Y. Zhou, N. Li, Q. Zhang, F. Han, Y. Xiao, P. Chow, W. Yang, V. V. Struzhkin, Y. Zhao, and H.-k. Mao, Emergent superconductivity in an iron-based honeycomb lattice initiated by pressure-driven spin-crossover, Nat. Commun. **9**, 1914 (2018).